ACS APPLIED MATERIALS & INTERFACES

Research Article

www.acsami.org

Effect of Crystallinity on Thermal Transport in Textured Lead Zirconate Titanate Thin Films

Ronnie Varghese,*[,†] Hari Harikrishna,[‡] Scott T. Huxtable,[§] W. T. Reynolds, Jr.,[†] and Shashank Priya[∥]

[†]Department of Materials Science, Virginia Tech, Blacksburg, Virginia 24061, United States

[‡]Department of Engineering Science and Mechanics, Virginia Tech, Blacksburg, Virginia 24061, United States

[§]Department of Mechanical Engineering, Virginia Tech, Blacksburg, Virginia 24061, United States

[∥]Center for Energy Harvesting Materials and Systems (CEHMS), Bio-inspired Materials and Devices Laboratory (BMDL), Virginia Tech, Blacksburg, Virginia 24061, United States

ABSTRACT: We demonstrate the use of the time domain thermoreflectance (TDTR) technique towards understanding thermal transport in textured $Pb(Zr,Ti)O_3$ (PZT) thin films grown by a sol-gel process on platinized silicon substrates. PZT films were grown with preferred crystallographic orientations of (100), (110), and (111). Grain orientation was controlled by manipulating the heterogeneous nucleation and growth characteristics at the interface between the film and the underlying Pt layer on the substrate. TDTR was used to measure both the PZT film thermal conductivity and the interface thermal conductance between the PZT and Pt as well as that between the PZT and an Al thermoreflectance layer evaporated on the PZT surface. We find a hierarchical dependence of thermal conductivity on the crystallographic orientation of the PZT films and observed differences in the thermal conductances between the Al-PZT and PZT-Pt interfaces for a varying degree of preferred orientations (100), (110), and (111). Thus, the technique based upon nanoscale thermal measurements can be used to delineate PZT samples with different crystallographic orientations. The thermal conductivities of the PZT films with different crystal orientations were in the range of 1.45−1.80 W m^{-1} K^{-1}. The interface thermal conductance between the PZT and Pt layer was in the range of 30−65 MW m^{-2} K^{-1}, while the conductance between the Al layer and PZT was in the range of 90−120 MW m^{-2} K^{-1}. These interfacial conductances exhibit significant correlations to the texture of the PZT film and elemental concentration and densities at those interfaces.

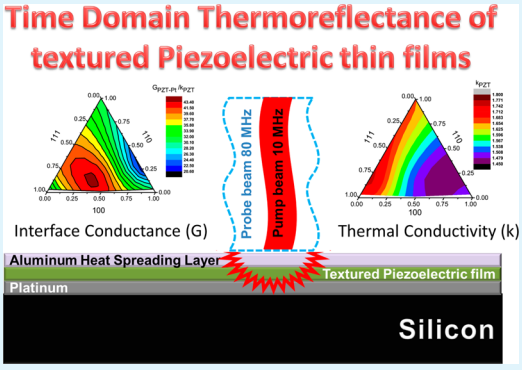

KEYWORDS: *thin films, thermal conductivity, thermal conductance, interface properties, texturing*

INTRODUCTION

Crystallographic texturing of $Pb(Zr,Ti)O_3$ (PZT) thin films on platinized Si substrates ($Pt/Ti/SiO_2/Si$) has been studied extensively, and various mechanisms related to the origin of the preferred orientation have been proposed in the literature.[1−9] An important factor in the nucleation and growth of a preferentially oriented PZT film on platinized Si is the interaction of the PZT precursors with the Pt layer. The boundary conditions at the PZT-Pt interface drive the degree of texturing that can be achieved in the annealed PZT films. Prior research has investigated the role of interfacial transient phases of an intermetallic Pt-Pb,[1,3,5] pyrochlore $Pb_2(Zr,Ti)_2O_6$,[5−7] permanent buffer, or seed layers of $PbTiO_3$,[2,4,8] TiO_2,[9] ZrO_2,[9] and PbO[1] concentration gradients on the evolution of texture. Even though the deterministic criterion controlling the magnitude of texture degree remains a debatable subject, the role of interfacial heterogeneity is indisputable and paramount for the nucleation and growth of a preferentially oriented PZT film. Few techniques are capable of detecting nanometer scale anomalies at a buried interface. We report the use of a thermo-optic probing technique to evaluate the thermal properties of PZT films and its interfaces, correlate them to crystalline orientation, and finally shed some light on probable causes to the trends observed in the properties.

In a prior study, we characterized the phase and orientation of sol-gel derived $Pb(Zr_{0.6}Ti_{0.4})O_3$ thin films and developed the temperature−time−transformation (TTT) diagrams illustrating the correlation between the synthesis parameters and crystallinity. Analytical models were developed to utilize the TTT diagrams effectively.[10] Building upon the earlier study, we investigate here the role of interfacial heterogeneity in the PZT films that could shed light on the mechanism responsible for development of texture. Various characterization techniques with increasing sensitivity including optical (ellipsometry and Raman) characterization, high resolution binding energy X-ray photoelectron spectroscopy, and high resolution transmission

Received: January 23, 2014
Accepted: April 1, 2014
Published: April 1, 2014

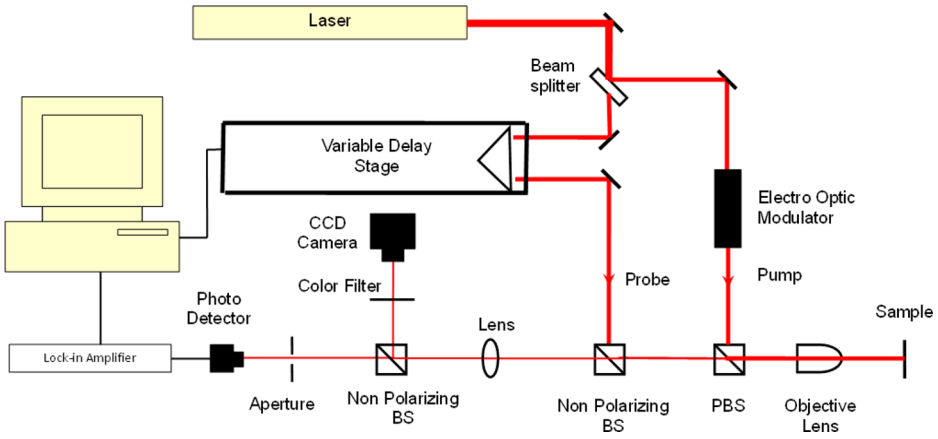

Figure 1. Schematic diagram of the TDTR system. The pump beam heats the surface of the sample, and the time-delayed probe beam monitors changes in temperature at the sample surface. Thermal conductivity and interface thermal conductance are extracted by comparing the experimental data with an analytical thermal model.

electron microscopy (HR-TEM) were utilized to study the interface between PZT and Pt, but no definitive correlations to an interfacial heterogeneity were found. To augment this characterization work, we use an optical technique called the time domain thermoreflectance (TDTR) to measure the interface thermal conductance, G, between the textured PZT films and the underlying Pt layer, along with the interface thermal conductance between the PZT and an Al layer that is evaporated on the PZT films. We use aluminum for the TDTR measurements since Al has the largest thermoreflectance coefficient near 800 nm radiation. We also use TDTR to simultaneously extract the thermal conductivity, k, of the textured PZT films. The variation in the magnitude of thermal conductance could be utilized for inferring the structural changes occurring at the interface.

Thermal conductivity, k, describes the ability of a material to transport heat, while the ability to transfer heat across an interface can be quantified in terms of an interface thermal conductance, G, which is simply the ratio of heat flux to the temperature drop across the interface. Typical values for G at metal/non-metal interfaces in intimate contact are often on the order of 10−100 MW m^{-2} K^{-1}, while metal/metal interfaces can have G in the range of 0.1−1 GW m^{-2} K^{-1}.[11,12] Electron transport dominates heat conduction in metals, while quantized lattice vibrations called phonons control heat conduction in non-metals. Metal/metal interfaces have a large interface thermal conductance due to good coupling of electrons across the interface, whereas the weaker coupling between the electrons in a metal and the phonons in a non-metal lead to lower interface thermal conductance at metal/non-metal interfaces. In the latter case, thermal energy can be transferred either by direct coupling between electrons in the metal and the phonons in the non-metal or via electron-phonon coupling within the metal followed by phonon−phonon coupling at the metal/non-metal interface.[13]

There have been a few recent studies where groups have examined the influence of crystal orientation on interface thermal conductance. Hopkins et al.[14] used TDTR to examine the thermal conductance at Al/Si and Al/sapphire interfaces with different Si and sapphire substrate orientations. They found that the interface thermal conductance for the sapphire samples (trigonal unit cell) showed a strong dependence on the crystal orientation while that was not the case with silicon samples (diamond cubic unit cell). The interface thermal conductance dependence on the crystal orientation in the Al/sapphire samples was attributed to the anisotropy in the Brillouin zone and subsequent changes in the phonon velocities with crystallographic direction in the sapphire. Costescu et al.[15] also used TDTR to measure the interface thermal conductance of TiN:MgO (001) and TiN:MgO (111), and they found no dependence on the crystallographic orientation. More recently, Duda et al.[16] used classical molecular dynamics simulations to study the influence of crystallographic orientation on the interface thermal conductance. They found that the thermal conductance at interfaces between two cubic materials was independent of crystallographic orientation, while the conductance between a face centered cubic material and a tetragonal material had a dependence on the orientation.

With TDTR, we find a hierarchical dependence of thermal conductivity on the crystallographic orientation of the PZT films and observed differences in the thermal conductances between the Al-PZT and PZT-Pt interfaces for a varying degree of preferred orientations, (100), (110), and (111). Understandably, the top Al-PZT interface thermal conductance was defined by the Al film growth on PZT, and the bottom PZT-Pt interface thermal conductance was dependent on the nucleation and growth of different PZT textures on Pt. To the best of our knowledge, this work is the first implementation of such an approach to study the properties of a textured piezoelectric thin film and its interfacial heterogeneity.

SAMPLE PREPARATION AND CHARACTERIZATION

The PZT thin film (Zr/Ti = 60/40) samples were synthesized by sol-gel processing as described in detail elsewhere.[10] With this technique, a series of films were synthesized and crystallized to achieve varying percentages of crystallographic orientations (111), (110), and (100). The crystallographic orientation and thickness of the samples were determined by Bragg-Brentano mode X-ray diffraction (Phillips Xpert Pro) and variable angle spectroscopic ellipsometry (J.A. Woollam), respectively. All of the samples had a rhombohedral crystal structure at room temperature. Transmission electron microscopy (TEM) was performed with an FEI Titan 300. Samples for TEM were prepared using a focused ion beam from an FEI Helios 600 NanoLab. Raman spectra were collected using a Jobin-Yvon T6400 Triplemate with 514.5 nm radiation. GI-XRD data were collected on a Bruker D8 Advance system with

an incident Goebel mirror having a 4 degree Soller slit and 0.6 mm exit slit. The diffracted beam side of the diffractometer was equipped with an equatorial Soller slit (0.2° divergence) and LynxEye detector in 0d mode. Data were collected using 2θ scans with fixed grazing incidence (either 4° or 6° incident angle).

EXPERIMENTAL MEASUREMENTS WITH TDTR

The time domain thermoreflectance (TDTR)[17−20] set up, as shown in Figure 1, relies on the fact that the reflectivity of aluminum has a measurable dependence on temperature. We used a Ti:sapphire mode-locked laser to produce a series of ∼100 fs optical pulses with a wavelength of 800 nm at a repetition rate of 80 MHz. These laser pulses are then split into two separate beams, which are referred to as the "pump" and "probe" beams. The pump beam is modulated at 10 MHz using an electro-optic modulator, and this beam is used to heat the sample. The surface of the sample is coated with a thin layer of aluminum (Al), as Al exhibits a relatively large change in reflectivity with temperature at 800 nm.[21] The probe beam was focused at the same location on the sample as the pump, and the reflected probe beam was directed to the photo detector. Thus, the intensity of the reflected probe beam was proportional to the surface temperature. A lock-in-amplifier recorded the in-phase (V_{in}) and out-of-phase voltages (V_{out}) from the photo detector. The arrival time of the probe beam at the sample was controlled with a mechanical delay stage. The system can measure the thermal decay of a sample with picosecond time resolution for delay times up to 3 ns. The $1/e^2$ diameters of the pump and probe beam were ∼25 μm. Since the penetration depth of the thermal wave was much smaller than the diameters of the pump and probe beams, the heat flow was predominantly one-dimensional through the sample and the measured thermal conductivity was in the direction normal to the sample surface.

The ratio of the in-phase and out-of-phase voltages was used to account for the non-idealities such as the change in the pump−probe overlap or defocusing of the probe beam. Our experimentally measured ratio was then compared with an analytical thermal model of the layered sample structure.[20,22] The thermal model starts with the frequency domain solution to the heat diffusion equation for the surface temperature of a semi-infinite sample under periodic heating from a point source. The solution to the heat equation is generalized for the layered geometry of the samples, and it is also solved in cylindrical coordinates for heating and temperature measurements by a Gaussian shaped laser. The ratio of the real and imaginary parts of the solution for the temperature rise at the sample surface corresponds to the ratio of the in-phase and out-of-phase voltages measured by the lock-in. The thermal model utilized is multipart and is described in detail by Cahill,[20] but briefly, the real and imaginary parts of the solution are given as

$$\mathrm{Re}[\Delta R_M(t)] = \frac{dR}{dT}\sum_{m=-M}^{M}\left(\Delta T\left(\frac{m}{\tau}+f\right)+\Delta T\left(\frac{m}{\tau}-f\right)\right)\exp(i2\pi mt/\tau) \quad (1)$$

$$\mathrm{Im}[\Delta R_M(t)] = -i\frac{dR}{dT}\sum_{m=-M}^{M}\left(\Delta T\left(\frac{m}{\tau}+f\right)-\Delta T\left(\frac{m}{\tau}-f\right)\right)\exp(i2\pi mt/\tau) \quad (2)$$

where ΔT is the temperature distribution at the sample surface measured by the probe beam, dR/dT is the thermoreflectance of the surface layer, f is the modulation frequency of the pump beam, t is time, and τ is the time between laser pulses. The temperature distribution at the surface depends on the thickness, thermal conductivity, and heat capacity of each layer in the model. The unknown parameters (k and/or G) in the model are then adjusted until satisfactory matching is found between the results from the model and the thermoreflectance measurements. The model requires the thickness, heat capacity, and thermal conductivity of each layer of the sample, and the details of the sample structure are given in Table 1.

Table 1. Composition, Orientation, and Dimensions of the Layers in the Synthesized Samples

layer	parameter	detail
Al	thickness (nm)	30
PZT	sample	$PbZr_{0.6}Ti_{0.4}O_3$ sol-gel
	orientation	(100), (110), (111)
	thickness (nm)	60−80
Pt	orientation	(111)
	thickness (nm)	150
Ti	thickness (nm)	10
SiO_2	thickness (nm)	300
Si	thickness (mm)	0.5

The thermal conductivities of the aluminum and platinum films were measured using the Wiedemann-Franz law and were found to be 180 and 70 W m^{-1} K^{-1}, respectively. The aluminum value was reduced slightly from its bulk values, since the film was thin. The thermal conductivities of the titanium and oxide layers and the heat capacities of all the layers except PZT were taken to be the same as the bulk values. The heat capacity of the PZT layer was assumed to be 2.4 MJ/(m^3·K) (with thin film density assumed to be equivalent to the bulk and using specific heat measurements performed on similar PZT materials by Lang et al.).[23]

With our sample configuration, we have five unknowns in the thermal model: the interface thermal conductance between aluminum and PZT, G1, the thermal conductivity of the PZT layer, k_{PZT}, the interface thermal conductance between PZT and platinum, G2, the interface thermal conductance between platinum and titanium, G3, and the interface thermal conductance between Ti and the oxide layer, G4. The interface thermal conductance at metal/metal interfaces is on the order of several hundred MW m^{-2} K^{-1}, beyond the range of the sensitivity of our measurements; thus, we can ignore G3 in this analysis.[12] To further reduce the number of unknowns, we examined a reference sample without the PZT layer and found the interface thermal conductance between titanium and the oxide layer, G4, to be ∼110 MW m^{-2} K^{-1}. The remaining three unknowns, G1, k_{PZT}, and G2, each affect the data (i.e., the ratio of the in-phase to out-of-phase voltage as a function of delay time) in a unique manner. In the model, G1 changes the radius of curvature of V_{in}/V_{out} below delay times of ∼0.5 ns, while G2 offsets the amplitude of the signal by an approximately constant value, and k_{PZT} causes an offset at short delay times and changes the radius of curvature at longer delay times (∼3 ns). This independence between the effects allows us to find a unique best fit even when we have multiple unknowns. Thus, we find that there is a unique combination of the three parameters that provides the best fit between the model and the experimental data, as shown in Figure 2. For each sample, we measured the values at a minimum of three different locations and found agreement within 3% across each individual sample.

RESULTS

The pyrolysis and annealing temperatures and times along with the resulting texturing, i.e., the relative crystallographic orientations, of the sol-gel PZT thin films are summarized in Table 2. From the texturing data, we can observe the following trends: (a) no pyrolysis and low thermal budget in annealing leads to (110), (b) low pyrolysis and high annealing thermal budgets provide (111), and (c) high pyrolysis and low annealing thermal budgets favor (100) texture. An XPS depth profile (Figure 3a) showed decreasing amounts of Pb, Zr, Ti, and O with depth while Pt was found to increase with depth. Interestingly, because of the surface roughness of the sputter crater created by the Argon sputter gas's unequal sputtering rate of elements in PZT, the Pt was detected at the surface and masks the Ti detection. Therefore, the detection of an interfacial seeding layer was ruled out by this technique.

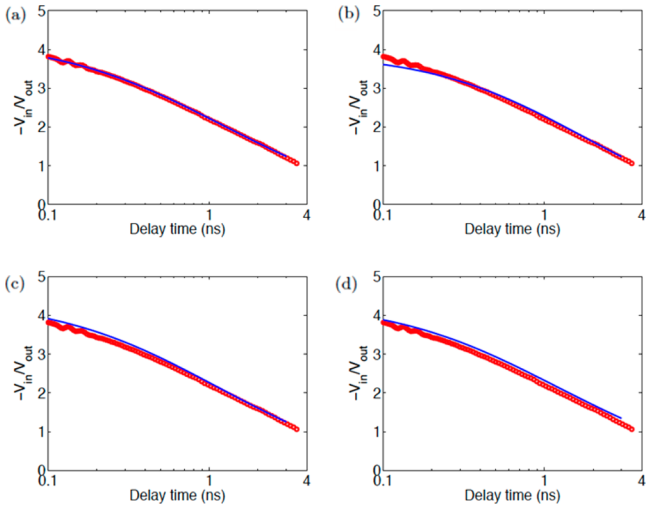

Figure 2. Sensitivity analysis for sample 64. In (a), the data are compared with the best fit model, while in (b) through (d) one parameter is changed, and the other two unknowns are kept at the best-fit value. (a) The best fit with all three unknown parameters, G1 = 110 MW m^{-2} K^{-1}, k_{PZT} = 1.6 W m^{-1} K^{-1}, and G2 = 60 MW m^{-2} K^{-1}. (b) If G1 is increased by less than 10% to 120 MW m^{-2} K^{-1}, the fit is clearly poor at short delay times; (c) if k is increased by ∼10% to 1.75 W m^{-1} K^{-1}, the fit is poor at short and intermediate times; (d) if G2 is increased by ∼15% to 70 MW m^{-2} K^{-1}, the fit is poor for all delay times.

Variable angle spectroscopic ellipsometry (VASE) data was collected off the samples, and the resulting models of the optical dispersion of the refractive index (n) and absorption coefficient (K) dispersion across wavelengths of 300−800 nm did not reveal any interfacial layer. However, as mentioned in the next section, there were optical dispersion variations with respect to crystallographic orientation. Raman spectral analysis (Figure 3c) of three highly textured samples showed minor differences only in A_1(2TO) mode which cannot be attributed to the crystallographic orientations.[24] Souza Filho et al.[24] observed that Raman spectra for rhombohedral compositions Zr = 0.54−0.6 were unchanged and had no distinguishing features.

TDTR measurements from the textured PZT samples listed in Table 2 were modeled as mentioned previously to provide the results in Table 3. From the data in Table 3 and the ternary thermal conductivity plot shown in Figure 4a, we find that the thermal conductivity of all of the PZT thin film samples falls within the range of 1.45−1.80 W m^{-1} K^{-1}. These thermal conductivity values are in line with other measurements on similar bulk PZT materials reported in the literature. Kallaev et al. examined two types of PZT ceramics and found k ∼ 1.35 for PKR-8 and k ∼ 1.77 W m^{-1} $K^{-1}$for PKR-7M at 300 K.[25] Rivera-Ruedas et al.[26] synthesized a series of PZT samples by mechanochemical activation of powder mixtures followed by thermal treatment. They found a larger range of thermal conductivity values with k between 0.55 and 2.1 W m^{-1} K^{-1}at room temperature, and no obvious trends were observed in thermal conductivity with the composition of the PZT or Pb oxide source. The variation in the thermal conductivity was attributed to the difference in microstructure and porosity. A variety of other bulk crystalline perovskite ferroelectric materials, including $NaNbO_3$ and $Pb(Mg_{0.33}Nb_{0.67})O_3$, exhibit similarly low thermal conductivity values in the range of 1−3 W m^{-1} K^{-1}, while others (e.g., $BaTiO_3$, $KNbO_3$, $PbTiO_3$, and $KTaO_3$) have slightly larger conductivity in the range of 3−15 W m^{-1} K^{-1} at room temperature.[27,28] While the absolute error in the thermal conductivity values is estimated to be ∼15%, the relative uncertainty between the samples should be considerably less. For example, much of the absolute error is a result of uncertainties in the Al and Pt film properties, and any errors in these values will affect all of the samples in the same manner (the Al films were evaporated on all of the samples simultaneously in one run, so we expect that the Al films on different samples will have nearly identical thickness). For data repeatability, each data point was corroborated by a 2nd batch of Al deposited PZT thin film fragment from the original thin film sample. Finally, the small spread in results we obtain on samples with similar crystal orientations indicates the precision of our measurements.

Figure 4b,c shows the ternary plots of the interface thermal conductance for G1 and G2 along with each conductance normalized to the thermal conductivity of the PZT layer (G/k). From the G1 ternary plot (Figure 4b), all measurements fall within a range of 90−120 MW m^{-2} K^{-1}. G1 trend varied as (100) > (111) > (110), while G1/k trend varied as (100) > (110) ∼ (111). The largest conductance values, albeit by a small yet consistent margin, are for samples with significant fraction of (100) orientation. The smallest G1 values were for samples with large fractions of (110) orientation. From the G2

Table 2. X-ray Diffraction Analysis Results for the PZT Samples

					thermal budget		orientation		
sample no.	pyrolysis temperature (°C)	pyrolysis time (min)	annealing temperature (°C)	annealing time (min)	pyrolysis	annealing	(100), %	(110), %	(111), %
4D	250	1.5	625	60	375	37 500	72	28	0
64	300	3	675	45	900	30 375	77	23	0
67	300	3	725	30	900	21 750	97	3	0
6A	300	3	775	15	900	11 625	93	7	0
62	250	1.5	675	75	375	50 625	0	9	91
72	250	1.5	800	60	375	48 000	0	3	97
76	250	1.5	750	60	375	45 000	0	4	96
4F	0	0	675	20	0	13 500	8	92	0
7B	0	0	650	45	0	29 250	6	94	0
81	0	0	700	45	0	31 500	0	100	0
68	300	3	775	45	900	34 875	39	20	41
7D	0	0	800	45	0	36 000	49	1	50

dx.doi.org/10.1021/am500482r | ACS Appl. Mater. Interfaces 2014, 6, 6748−6756

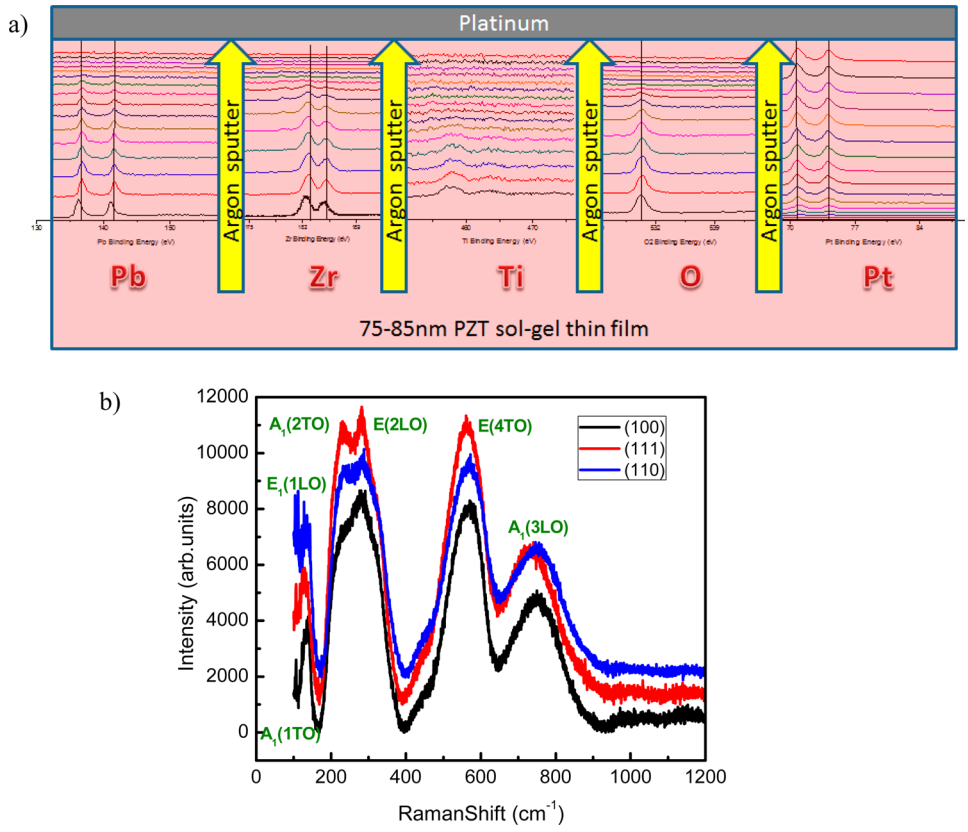

Figure 3. (a) High resolution binding energy XPS depth profiling of a PZT sol-gel thin film and (b) Raman shift data for the 3 highly textured PZT sol-gel thin films.

Table 3. TDTR Results from the PZT Samples

	orientation							
sample no.	(100), %	(110), %	(111), %	$G_{Al\text{-}PZT}$ or G1 (MW/m^2·K)	k_{PZT} (W/m·K)	$G_{PZT\text{-}Pt}$ or G2 (MW/m^2·K)	G1/k	G2/k
4D	72	28	0	110	1.45	30	75.86	20.69
64	77	23	0	110	1.45	30	75.86	20.69
67	97	3	0	110	1.50	45	73.33	30.00
6A	93	7	0	110	1.50	45	73.33	30.00
62	0	9	91	100	1.80	65	55.56	36.11
72	0	3	97	100	1.70	50	58.82	29.41
76	0	4	96	100	1.70	50	58.82	29.41
4F	8	92	0	90	1.65	50	54.55	30.30
7B	6	94	0	90	1.65	50	54.55	30.30
81	0	100	0	100	1.65	50	60.61	30.30
68	39	20	41	110	1.50	65	73.33	43.33
7D	49	1	50	120	1.50	65	80.00	43.33

ternary plot (Figure 4c), all measurements fall within a range of 30−65 MW m^{-2} K^{-1}. As our TDTR measurements were ex situ, transient intermediate phases of intermetallics or pyrochlore cannot be sensed. If PbO,[1,9] Ti-rich PZT (~$PbTiO_3$),[4,8] and ZrO_2[9] are seeding the (100) texture, then G2 should decrease with an increase in (100) orientation; however, this decrease in G2 would be small because any interfacial oxide layer here would be thin. For G2, no hierarchical trends were observed, but roughly even mixtures of (111) and (100) orientation provided the largest conductances.

DISCUSSION

We observed a ranking of the thermal conductivity with respect to the crystal orientation. The thermal conductivities of the samples that predominantly contain (111) orientation are greater than for the samples containing (100) orientation. The origin of this trend in thermal conductivity may be the anisotropy of the rhombohedral lattice. If the thermal conductivity is significantly greater in a particular crystallographic direction, it could cause films of different textures to exhibit different average thermal conductivities. To confirm this hypothesis, it is necessary to infer the principal thermal conductivities from the textured films and show that they conform to the rhombohedral symmetry constraint, $k_{11} \sim k_{22} < k_{33}$. To do this, we assumed that the measured thermal

dx.doi.org/10.1021/am500482r | ACS Appl. Mater. Interfaces 2014, 6, 6748−6756

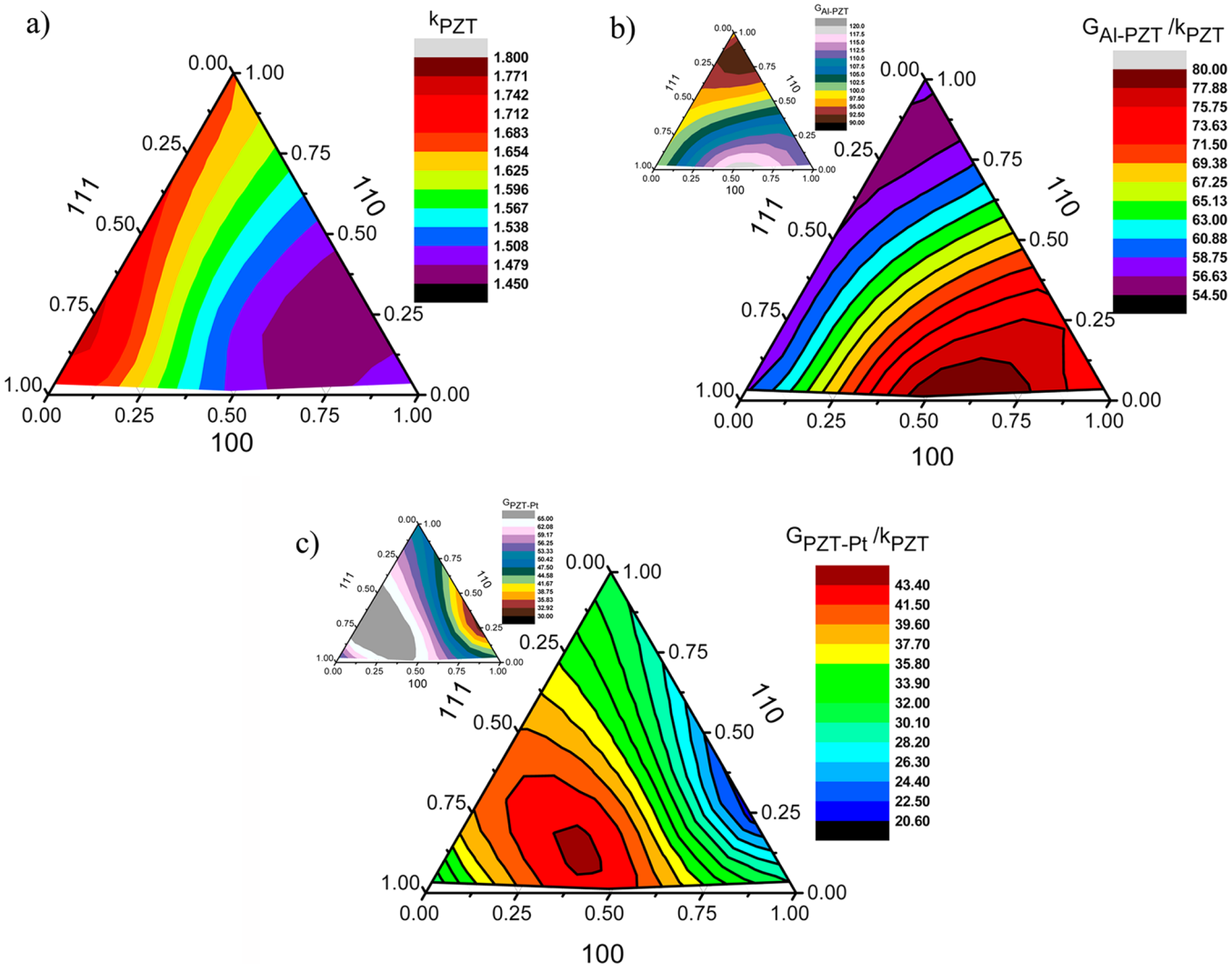

Figure 4. Ternary contour plots of (a) thermal conductivity of PZT, (b) G1/k or $G_{Al\text{-}PZT}/k_{PZT}$, (inset : G1 or $G_{Al\text{-}PZT}$), and (c) G2/k or $G_{PZT\text{-}Pt}/k_{PZT}$ (inset: G2 or $G_{PZT\text{-}Pt}$) vs. crystallographic orientation.

conductivity of each sample can be expressed as a weighted average of contributions from the three observed types of texture designated as k_{111}, k_{100}, and k_{110}. That is, $k_{(PZT,\ sample)} = w_{111}\ k_{111} + w_{100}\ k_{100} + w_{110}\ k_{110}$ where the "w_{ijk}" represents the fractions of the corresponding crystal orientation in each sample. From the measured w_{ijk} values for all of the samples, best fit values were obtained for the thermal conductivities at end points, k_{111} = 1.71, k_{100} = 1.43, and k_{110} = 1.65. These values can be transformed to the principal coordinate system of the thermal conductivity (a second rank tensor property) to yield k_{11}, k_{22}, and k_{33}. The principal values of the thermal conductivities are k_{11} = 1.20, k_{22} = 1.54, and k_{33} = 1.71. The point group symmetry requires the first two to be identical and less than the third. While the latter trend is confirmed, the former's nonconformity suggests this observed variation in the thermal conductivity with film texture is caused by factors other than simply crystal anisotropy. The Bragg-Brentano geometry used in quantifying the relative textures of our thin films has incident and diffracted beams that are equivalently varied during a measurement and thus therefore measures diffraction planes that are parallel during the entire measurement. Thick textured PZT thin films are known to grow with columnar grains oriented parallel to the sample normal,[29] and our thin films do possess some columnar grains (discussed later in Figure 7a). The effect of these columnar grains on the fractions of the corresponding crystal orientation "w_{ijk}", in each sample as measured in Bragg-Brentano XRD diffractions, explains the $k_{11}-k_{22}$ disparity.[30]

Next, we used the proportionality of the refractive index of a material to its density[31] to explain the trends in thermal conductivity. The trends of refractive index and extinction coefficient at 633 nm with orientation are shown in Figure 5a,b. Intuitively, thermal conductivity of a material is proportional to its density. From Figure 5a, the trend in refractive index mimics that of thermal conductivity—high thermal conductivity for high refractive index of (111) textures. The thermal conductivity is proportional to (110) and inversely proportional to (100) fractions. (111) texture has high packing density while (100) has the lowest free energy and thereby high growth rate.[32] The faster (100) growth rate can lead to films with more grain boundaries and porosity. The high k values at low (111) and high (110) may be explained by the low extinction coefficient K at those textures (Figure 5b). Low K is often attributable to low band gap defects and low oxygen vacancies.[31] Oxygen vacancies[33,34] and grain boundaries[35] induce phonon scattering. Competing heterogeneous and homogeneous nucleation and

dx.doi.org/10.1021/am500482r | ACS Appl. Mater. Interfaces 2014, 6, 6748−6756

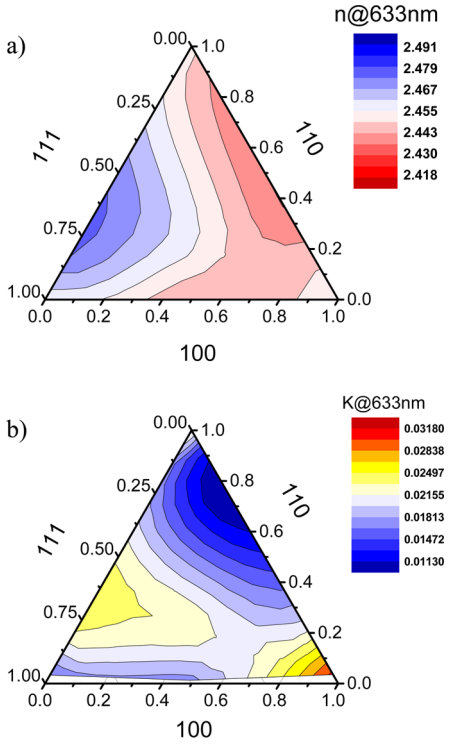

Figure 5. Ternary contour plots of (a) refractive index and (b) extinction coefficient at 633 nm wavelength.

growth mechanisms lead to (110) orientation development[36] and therefore the latter texture's direct proportionality to thermal conductivity.

The surface density for the rhombohedral unit cell vs. crystallographic orientation are tabulated in Table 4 above and

Table 4. Surface Density of the Crystallographic Planes for Rhombohedral PZT

atoms/cm^2	(100)	(110)	(111)
Pb atoms/area	6.157×10^{14}	4.367×10^{14}	3.601×10^{14}
Ti atoms/area		1.747×10^{14}	2.881×10^{14}
Zr atoms/area		2.620×10^{14}	4.321×10^{14}
O atoms/area	6.157×10^{14}	4.367×10^{14}	1.080×10^{15}

trends are as (111) ≫ (110) > (100). Clearly, (100) has a higher Pb surface density than (111) and (110). From an electroneutrality point of view, based on the surface density data, (100) planes are charge neutral (summation of the products of the surface density with the valence of each element in Table 4) while (110) is more charged than (111). Heat spreading thin film Al's growth on these charged surfaces will be impacted, and therefore, G1 trends should be dependent on PZT's elemental surface densities. The thermal conductivity of the elements in our Al-PZT-Pt-Ti system trend as Al ≫ Pt > Pb > Ti > Zr ⋙ O. Pb and Ti surface density and charge neutrality maps with respect to orientation were calculated and presented in Figure 6a–c. From these contours, G1 is found to be proportional to Pb surface density and inversely to Ti surface density and charge neutrality. (110)'s highest charge non-neutrality and (100)'s high Pb surface density and low Ti surface density might explain the lowest and highest G1 observed, respectively.

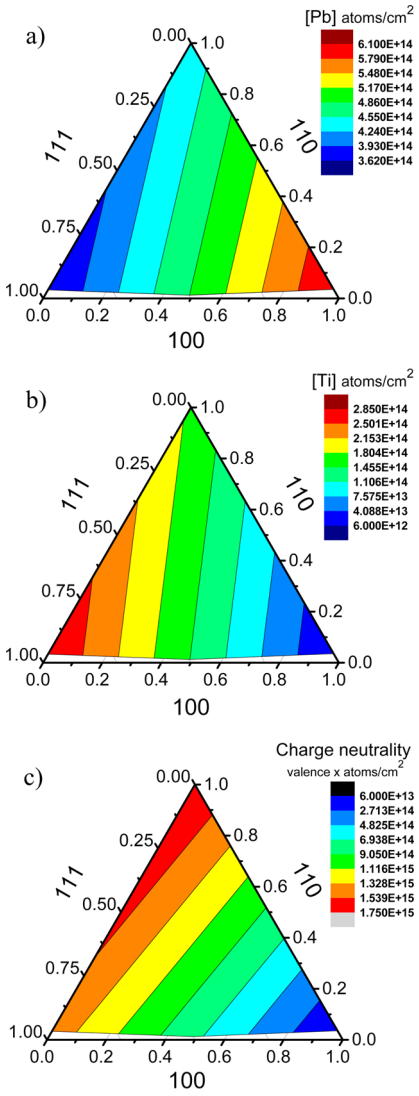

Figure 6. Ternary contour plots of (a) Pb surface density, (b) Ti surface density, and (c) charge neutrality for the samples.

The G2 trends with respect to texture were not as straightforward as G1's, and therefore, the causatives were equally intricate. An earlier study[37] using seed layers of $(TiO_2)_x(PbO)_y$ may help explain Figure 4c. They observed that Ti rich seed layers generated (111) and Pb rich seed layers produce (100) texture. From the surface density plots Figure 6a,b, our Ti rich zone has (111) and Pb rich has (100) orientations, respectively. Ti rich seed layers like TiO_2 seed layers[9,38] and Ti–Pt,[36] formed by Ti diffused up to Pt surface, are known to produce (111) textures. To test the Ti-rich hypothesis, a highly textured (111) sample #62 was used for high resolution TEM analysis. In the cross-sectional TEM micrograph shown in Figure 7a, an abrupt transition from Pt to PZT is evident. No evidence was found for a seeding or intermetallic layer between Pt and PZT that could affect the evolution of texture in PZT films. However, the energy dispersive spectroscopy (EDS) maps (Figure 7b,c) show that the interface between the PZT and Pt appears to be Ti rich and slightly Zr deficient. The segregation of Ti at the PZT-Pt interface has been observed earlier[7,39] where it was attributed to the Ti flow (and Zr flow away) to the growth interface where heterogeneous nucleation and growth of the crystalline PZT

dx.doi.org/10.1021/am500482r | ACS Appl. Mater. Interfaces 2014, 6, 6748–6756

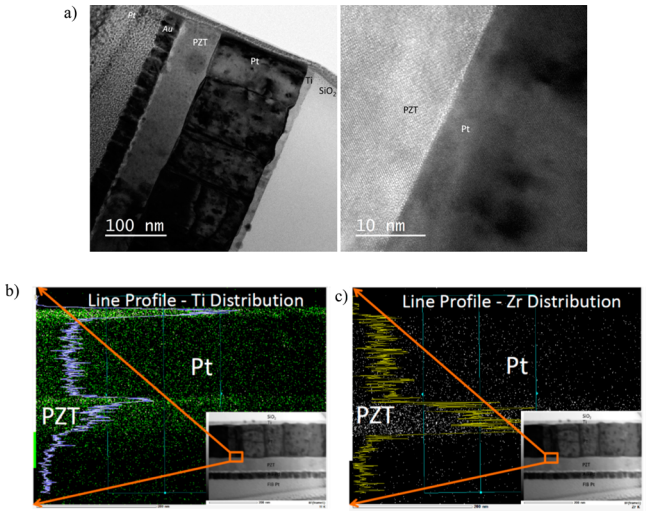

Figure 7. (a) High resolution TEM of a highly textured PZT sol-gel thin film. The Au and Pt on the left side of the left panel were added to the sample during the lift-out process in preparation for the TEM. EDS maps show (b) Ti distribution and (c) Zr distribution across the PZT-Pt interface.

phase occurs. As per binary phase diagrams of Pt-Pb, Pt-Zr, and Pt-Ti,[40] please note that only Ti and Zr can dissolve in Pt while all three, Pb, Ti, and Zr, will form intermetallics with Pt.

We turned to GI-XRD to further investigate the trends observed in the G2 plot. GI-XRD results confirmed standard XRD results for all textured films except for the mixed texture films 64, 4D, 68, and 7D. Samples 64 and 4D have the lowest G2 and the highest amount of a phonon scattering oxygen deficient $Pb_2(Zr,Ti)_2O_6$ phase (JCPDS 26-0142) pyrochlore.[7,41] Meanwhile, samples 68 and 7D have the largest G2 interface conductances (the source of the maxima observed in the ternary plots, Figure 4c) and are mixtures of 40−50% of (100) with (111) orientation while showing the presence of Pt-Ti alloy (Pt-Ti_3; JCPDS 18-0979 and 07-0353). At certain mixes of seed layers of $(TiO_2)_x(PbO)_y$ all three (100), (110), and (111) orientations can be formed[37] and may be the source of sample 68 and 7D's textures. When competing textures of (111) and (100) nucleate, there is the possibility of island type PZT growth and exposure to bare Pt.[37] This "exposed" Pt might be forming the Pt-Ti alloy and causing the high G2 conductance. This Ti[42] might be responsible for the (111) texture development despite the (100) conducive thermal budget employed on these two samples.

In addition to the textured PZT films, we also examined a 1 micrometer thick amorphous sample. In this thick sample, the heat pulses from the laser do not penetrate beyond the PZT layer and therefore there are only two unknown parameters, G1 and k_{PZT}. As one would expect, the thermal conductivity of this amorphous sample is considerably smaller than the conductivity for the crystalline films with a k of 0.53 W m^{-1} K^{-1}. Interestingly, despite the significant change in the crystal structure of the PZT film and, subsequently, the film thermal conductivity, the interface thermal conductance, G1, was found to be similar to previous measurements at 100 MW m^{-2} K^{-1}. One possible reason for the lack of change in G1 with the large change in PZT film structure could be that this interface thermal conductance is controlled by the electron-phonon coupling within the aluminum rather than phonon−phonon interactions across the interface.

CONCLUSIONS

In this Article, we report the use of time domain thermoreflectance to examine the thermal conductivity and interface thermal conductance for a series of textured PZT samples grown by the sol-gel process. We find that the thermal conductivity of the PZT films ranges from 1.45 to 1.80 W m^{-1} K^{-1} and has a clear dependence on the film texture. The trends in thermal conductivity are exemplified by the anisotropy of the rhombohedral lattice within the PZT films and their optical properties. The interface thermal conductance between the PZT and Pt layer was in the range of 30−65 MW m^{-2} K^{-1}, while the conductance between the Al layer and PZT was in the range of 90−120 MW m^{-2} K^{-1}. The thermal conductance at the top Al/PZT interface showed a substantial dependence on the crystal orientation and trended significantly with PZT's elemental surface densities and charge neutrality. Trends in thermal conductance at the bottom Pt/PZT interface were not hierarchical and varied distinctly on surface density variations, pyrochlore phase, elemental segregation at interfaces, and alloy formation.

AUTHOR INFORMATION

Corresponding Author

*E-mail: ronniev@vt.edu.

Notes

The authors declare no competing financial interest.

ACKNOWLEDGMENTS

The authors gratefully acknowledge the financial support from *Air Force Office of Scientific Research (AFOSR)* through the *Young Investigator Program* and Office of Naval Research through CEHMS seed program. We are also greatly indebted to Reema Gupta for assistance with GI-XRD indexing, Shashank Gupta for valuable discussions, Charles Farley for the FTIR characterization work conducted at Department of Geosciences at Virginia Tech, Holger Cordes of Bruker-AXS for GI-XRD, Ashok Kumar for the Raman work conducted at University of Puerto Rico's Speclab, Deepam Maurya and Chris Winkler for the TEM micrographs, and Jerry Hunter of Nanoscale Characterization and Fabrication Lab at Virginia Tech for the XPS analysis.

REFERENCES

(1) Chen, S.-Y.; Chen, I. W. Temperature−Time Texture Transition of Pb(Zr1−xTix)O3 Thin Films: I, Role of Pb-rich Intermediate Phases. *J. Am. Ceram. Soc.* **1994**, *77*, 2332−2336.

(2) Potrepka, D. M.; Fox, G. R.; Sanchez, L. M.; Polcawich, R. G. Pt/TiO2 Growth Templates for Enhanced PZT films and MEMS Devices. *MRS Proc.* **2011**, *1299*, s02−04, DOI: 10.1557/opl.2011.53.

(3) Huang, Z.; Zhang, Q.; Whatmore, R. W. The Role of an Intermetallic Phase on the Crystallization of Lead Zirconate Titanate in Sol−Gel Process. *J. Mater. Sci. Lett.* **1998**, *17*, 1157−1159.

(4) Sanchez, L. M.; Potrepka, D. M.; Fox, G. R.; Takeuchi, I.; Polcawich, R. G. Improving PZT Thin Film Texture Through Pt Metallization and Seed Layers. *MRS Proc.* **2011**, *1299*, s04−09, DOI: 10.1557/opl.2011.254.

(5) Nittala, K.; Mhin, S.; Dunnigan, K. M.; Robinson, D. S.; Ihlefeld, J. F.; Kotula, P. G.; Brennecka, G. L.; Jones, J. L. Phase and Texture Evolution in Solution Deposited Lead Zirconate Titanate Thin Films: Formation and Role of the Pt[Sub 3]Pb Intermetallic Phase. *J. Appl. Phys.* **2013**, *113*, 244101−244111.

(6) Norga, G. J.; Fé, L.; Vasiliu, F.; Fompeyrine, J.; Locquet, J. P.; Van der Biest, O. Orientation Selection in Functional Oxide Thin Films. *J. Eur. Ceram. Soc.* **2004**, *24*, 969−974.

(7) Reaney, I.; Taylor, D.; Brooks, K. Ferroelectric PZT Thin Films by Sol-Gel Deposition. *J. Sol-Gel Sci. Technol.* **1998**, *13*, 813−820.
(8) Tyholdt, F.; Calame, F.; Prume, K.; Ræder, H.; Muralt, P. Chemically Derived Seeding Layer for {100}-textured PZT Thin Films. *J. Electroceram.* **2007**, *19*, 311−314.
(9) Zhu, C.; Chentao, Y.; Sheng, W.; Bangchao, Y. The Effects of the PbO Content and Seeding Layers upon the Microstructure and Orientation of Sol-Gel Derived PZT Films. *J. Mater. Sci.: Mater. Electron.* **2006**, *17*, 51−55.
(10) Varghese, R.; Williams, M.; Gupta, S.; Priya, S. Temperature-Time Transformation Diagram for Pb(Zr,Ti)O[Sub 3] Thin Films. *J. Appl. Phys.* **2011**, *110*, 014109−014110.
(11) Lyeo, H. K.; Cahill, D. G. Thermal Conductance of Interfaces Between Highly Dissimilar Materials. *Phys. Rev. B* **2006**, *73*, 144301.
(12) Gundrum, B. C.; Cahill, D. G.; Averback, R. S. Thermal Conductance of Metal-Metal Interfaces. *Phys. Rev. B* **2005**, *72*, 245426.
(13) Majumdar, A.; Reddy, P. Role of Electron-Phonon Coupling in Thermal Conductance of Metal-Nonmetal Interfaces. *Appl. Phys. Lett.* **2004**, *84*, 4768−4770.
(14) Hopkins, P. E.; Beechem, T.; Duda, J. C.; Hattar, K.; Ihlefeld, J. F.; Rodriguez, M. A.; Piekos, E. S. Influence of Anisotropy on Thermal Boundary Conductance at Solid Interfaces. *Phys. Rev. B* **2011**, *84*, 125408.
(15) Costescu, R. M.; Wall, M. A.; Cahill, D. G. Thermal Conductance of Epitaxial Interfaces. *Phys. Rev. B* **2003**, *67*, 054302.
(16) Duda, J. C.; Kimmer, C. J.; Soffa, W. A.; Zhou, X. W.; Jones, R. E.; Hopkins, P. E. Influence of Crystallographic Orientation and Anisotropy on Kapitza Conductance via Classical Molecular Dynamics Simulations. *J. Appl. Phys.* **2012**, *112*, 093515.
(17) Cahill, D. G.; Ford, W. K.; Goodson, K. E.; Mahan, G. D.; Majumdar, A.; Maris, H. J.; Merlin, R.; Phillpot, S. R. Nanoscale Thermal Transport. *J. Appl. Phys.* **2003**, *93*, 793−818.
(18) Cahill, D. G.; Goodson, K.; Majumdar, A. Thermometry and Thermal Transport in Micro/Nanoscale Solid-State Devices and Structures. *J. Heat Transfer-Trans. ASME* **2002**, *124*, 223−241.
(19) Huxtable, S. Time-Domain Thermoreflectance Measurements for Thermal Property Characterization of Nanostructures. In *Handbook of Instrumentation and Techniques for Semiconductor Nanostructure Characterization*; Haight, R.; Ross, F. M.; Hannon, J. B., Eds. World Scientific Publishing Co.: Hackensack, NJ, 2012; Chapter 13, pp 587−610.
(20) Cahill, D. G. Analysis of Heat Flow in Layered Structures for Time-Domain Thermoreflectance. *Rev. Sci. Instrum.* **2004**, *75*, 5119−5122.
(21) Wang, Y.; Park, J.; Koh, Y. K.; Cahill, D. G. Thermoreflectance of Metal Transducers for Time-Domain Thermoreflectance. *J. Appl. Phys.* **2010**, *108*, 043507.
(22) Feldman, A. Algorithm for Solutions of the Thermal Diffusion Equation in a Stratified Medium with a Modulated Heating Source. *High Temp.-High Pressures* **1999**, *31*, 293−298.
(23) Lang, S. B.; Zhu, W. M.; Ye, Z. G. Specific Heat of Ferroelectric Pb(Zr1-xTix)O-3 Ceramics Across the Morphotropic Phase Boundary. *J. Appl. Phys.* **2012**, *111*, 094102.
(24) Souza Filho, A. G.; Lima, K. C. V.; Ayala, A. P.; Guedes, I.; Freire, P. T. C.; Melo, F. E. A.; Mendes Filho, J.; Araújo, E. B.; Eiras, J. A. Raman Scattering Study of the PbZr_{1-x}Ti_{x}O_{3} System: Rhombohedral-Monoclinic-Tetragonal Phase Transitions. *Phys. Rev. B* **2002**, *66*, 132107.
(25) Kallaev, S. N.; Gadzhiev, G. G.; Kamilov, I. K.; Ornarov, Z. M.; Sadykov, S. A.; Reznichenko, L. A. Thermal Properties of PZT-Based Ferroelectric Ceramics. *Phys. Solid State* **2006**, *48*, 1169−1170.
(26) Rivera-Ruedas, G.; Ramirez-Lopez, L. M.; de Jesus, F. S.; Bolarin-Miro, A.; Munoz-Saldana, J.; Yanez-Limon, J. M. Thermal Characterization of PZT Ceramics Obtained by Mechanically Activated Mixed Oxides Using Different Pb Sources. *Int. J. Thermophys.* **2012**, *33*, 2366−2376.
(27) Zhu, D. M.; Han, P. D. Thermal Conductivity and Electromechanical Property of Single-Crystal Lead Magnesium Niobate Titanate. *Appl. Phys. Lett.* **1999**, *75*, 3868−3870.
(28) Tachibana, M.; Kolodiazhnyi, T.; Takayama-Muromachi, E. Thermal Conductivity of Perovskite Ferroelectrics. *Appl. Phys. Lett.* **2008**, *93*, 092902.
(29) Ledermann, N.; Muralt, P.; Baborowski, J.; Gentil, S.; Mukati, K.; Cantoni, M.; Seifert, A.; Setter, N. {1 0 0}-Textured, Piezoelectric Pb(Zrx, Ti1−x)O3 Thin Films for Mems: Integration, Deposition and Properties. *Sens. Actuators, A* **2003**, *105*, 162−170.
(30) Nittala, K.; Mhin, S.; Jones, J. L.; Robinson, D. S.; Ihlefeld, J. F.; Brennecka, G. L. In Situ X-ray Diffraction of Solution-derived Ferroelectric Thin Films for Quantitative Phase and Texture Evolution Measurement. *J. Appl. Phys.* **2012**, *112*, 104109.
(31) Varghese, R.; Pribil, G.; Reynolds, W. T., Jr.; Priya, S. Ellipsometric Characterization of Multi-Component Thin Films: Determination of Elemental Content from Optical Dispersion. *Thin Solid Films* **2014**, *550*, 239−249.
(32) Pronin, V. P.; Senkevich, S. V.; Kaptelov, E. Y.; Pronin, I. P. Features of the Formation of a Perovskite Phase in Thin Polycrystalline Pb(Zr,Ti)O_3 Films. *J. Surf. Invest.* **2010**, *4*, 703−708.
(33) Winter, M. R.; Clarke, D. R. Oxide Materials with Low Thermal Conductivity. *J. Am. Ceram. Soc.* **2007**, *90*, 533−540.
(34) Klemens, P. G. Phonon Scattering by Oxygen Vacancies in Ceramics. *Phys. B: Condens. Matter* **1999**, *263*−*264*, 102−104.
(35) Daly, B. C.; Maris, H. J.; Nurmikko, A. V.; Kuball, M.; Han, J. Optical Pump-and-Probe Measurement of the Thermal Conductivity of Nitride Thin Films. *J. Appl. Phys.* **2002**, *92*, 3820−3824.
(36) Tani, T.; Xu, Z.; Payne, D. A. Preferred Orientations for Sol-Gel Derived PLZT Thin Layers. *MRS Online Proc. Libr.* **1993**, *310*, 269.
(37) Hiboux, S.; Muralt, P. Mixed Titania-Lead Oxide Seed Layers for PZT Growth on Pt(111): A Study on Nucleation, Texture and Properties. *J. Eur. Ceram. Soc.* **2004**, *24*, 1593−1596.
(38) Muralt, P.; Maeder, T.; Sagalowicz, L.; Hiboux, S.; Scalese, S.; Naumovic, D.; Agostino, R. G.; Xanthopoulos, N.; Mathieu, H. J.; Patthey, L.; Bullock, E. L. Texture Control of PbTiO3 and Pb(Zr,Ti)O3 Thin Films with TiO2 Seeding. *J. Appl. Phys.* **1998**, *83*, 3835−3841.
(39) Muralt, P. Recent Progress in Materials Issues for Piezoelectric MEMS. *J. Am. Ceram. Soc.* **2008**, *91*, 1385−1396.
(40) Massalski, T. B., Okamoto, H., Ed. *Binary alloy phase diagrams*; ASM International: Materials Park, Ohio, 1990.
(41) Brooks, K. G.; Reaney, I. M.; Klissurska, R.; Huang, Y.; Bursill, L.; Setter, N. Orientation of Rapid Thermally Annealed Lead Zirconate Titanate Thin Films on (111) Pt Substrates. *J. Mater. Res.* **1994**, *9*, 2540−2553.
(42) Aoki, K. Effects of Titanium Buffer Layer on Lead-Zirconate-Titanate Crystallization Processes in Sol-Gel Deposition Technique. *Jpn. J. Appl. Phys. Part 2, Lett.* **1995**, *34*, 192−195.